



## LJMU Research Online

Shi, Z, Liu, S, Zhou, Y, Xing, X, Ren, X and Yang, Q

**Structure and properties of YAIO<sub>3</sub>/NbC heterogeneous nucleation interface: First principles calculation and experimental research**

<http://researchonline.ljmu.ac.uk/id/eprint/9834/>

### Article

**Citation** (please note it is advisable to refer to the publisher's version if you intend to cite from this work)

**Shi, Z, Liu, S, Zhou, Y, Xing, X, Ren, X and Yang, Q (2018) Structure and properties of YAIO<sub>3</sub>/NbC heterogeneous nucleation interface: First principles calculation and experimental research. Journal of Alloys and Compounds. 773. pp. 264-276. ISSN 0925-8388**

LJMU has developed **LJMU Research Online** for users to access the research output of the University more effectively. Copyright © and Moral Rights for the papers on this site are retained by the individual authors and/or other copyright owners. Users may download and/or print one copy of any article(s) in LJMU Research Online to facilitate their private study or for non-commercial research. You may not engage in further distribution of the material or use it for any profit-making activities or any commercial gain.

The version presented here may differ from the published version or from the version of the record. Please see the repository URL above for details on accessing the published version and note that access may require a subscription.

For more information please contact [researchonline@ljmu.ac.uk](mailto:researchonline@ljmu.ac.uk)

<http://researchonline.ljmu.ac.uk/>

## Structure and properties of YAlO<sub>3</sub>/NbC heterogeneous nucleation interface: First principles calculation and experimental research

Zhijun Shi <sup>a</sup>, Sha Liu <sup>a</sup>, Yefei Zhou <sup>a, b</sup>, Xiaolei Xing <sup>a, b</sup>, Xuejun Ren <sup>c</sup>, Qingxiang Yang <sup>a, \*</sup>

<sup>a</sup> State Key Laboratory of Metastable Materials Science & Technology, Yanshan University, Qinhuangdao 066004, PR China

<sup>b</sup> College of Mechanical Engineering, Yanshan University, Qinhuangdao 066004, PR China

<sup>c</sup> School of Engineering, Liverpool John Moores University, Liverpool L3 3AF, UK

### Abstract

The characteristics of YAlO<sub>3</sub>/NbC heterogeneous nucleation interface are strongly associated with the interfacial structure, electronic construction and properties. The lattice mismatch between low index crystal faces of YAlO<sub>3</sub> and NbC was calculated by using the Bramfitt two-dimensional lattice mismatch theory. The work of adhesion, interfacial energy and electronic structure of the YAlO<sub>3</sub>(001)/NbC(100) interface structures were calculated by the first principles method. The charge density difference, electron localization function and crystal orbits overlap population were adopted to analyze the charge transfer and bond characteristics. The microstructure of surfacing alloy was observed by transmission electron microscopy (TEM). The results show that, the two-dimensional lattice mismatch of YAlO<sub>3</sub>(001)-NbC(100) interface is 5.4%, which testifies that YAlO<sub>3</sub> can meet the lattice structure condition of being an effective heterogeneous nucleus of NbC. In all interface structures, the work of adhesion of C-O2 model is the largest ( $W_{ad}=6.558 \text{ J/m}^2$ ) and the interfacial energy of C-Y model is the smallest ( $\gamma=0.54 \text{ J/m}^2$ ). It can be confirmed that the C-Y interface structure is the most stable one, whose interfacial energy is the smallest. The chemical bonds between interface atoms of all models are major covalent bonds and few metal bonds. The calculation results indicate that YAlO<sub>3</sub>(001) slab and NbC(100) slab can form a stable interface structure. The TEM results verify that the rare earth compound in NbC particle is YAlO<sub>3</sub>. In addition, NbC growth encircling YAlO<sub>3</sub> and they are combined tightly. Therefore, YAlO<sub>3</sub> can act as the effective heterogeneous nucleus of NbC and refine it.

## 1. Introduction

Niobium carbide, due to its attractive properties such as high hardness, high elastic modulus, high melting point, chemical inertness, etc. has been applied in engineering fields [1]. As strengthening phase, NbC plays a major role in improving the strength of various alloy systems such as Cu-based alloy, Ni-based alloy, Fe-based alloy and so on [2-4]. Meanwhile, NbC is also widely used as a refiner to strengthen the materials, refine the grain size and improve the mechanical property of the alloys [5]. Zhang et al. [6] researched the behavior of NbC carbide in austenite, which indicates that NbC provide a superior coarsening resistance to austenite. Qin et al. [7] prepared the nano-NbC particle reinforced low-carbon a-Fe steels and found that the nano-NbC can refine the microstructure remarkably. Zhang et al. [8] researched the refinement mechanism of NbC on TiN, which reveals that NbC heterogeneous nucleation on TiC preferentially occurs on the (1 1 1) surface. Liu et al. [9] investigated the refinement mechanism of NbC on primary  $M_7C_3$  carbides in hypereutectic Fe-Cr-C alloy, in which the experimental and computational results demonstrate that NbC particle is the heterogeneous nucleus of primary  $M_7C_3$  carbide and thereby refines it. The researches [10,11] indicate that the refinement effect of NbC is related with its size closely, and the smaller its size is, the better the refinement is. Therefore, it is significant to further refine the NbC size during the process of alloy solidification. Because of the special electronic structure and physical property, heavy rare earth element Y is widely applied in industrial engineering, energy sources, electronics and other fields. The purification [12], modification [13,14] and refinement [15] effects of element Y in the alloys have been reported. Especially the element Y can form compounds with the impurities in alloys. During the process of solidification, because the interface between the compound containing element Y and the post-precipitated alloy phase is coherent, which indicates that the compound containing element Y can be heterogeneous nucleus of post-precipitated phase and then refine the microstructure of the alloy. Yang et al. [15] researched the effect of  $YAlO_3$  on microstructure and mechanical properties of Fe-based alloys, which reveals that  $YAlO_3$  can be the effective heterogeneous nucleus of austenite. Liu et al. [16] investigated the refinement of  $Y_2O_3$  on TiC, which indicates that  $Y_2O_3$  can act as the heterogeneous nucleus of TiC and refine it. The researches [17,18] indicate that element Y can form  $YAlO_3$  with element Al and element O in the molten pool of Fe-based alloy. So whether  $YAlO_3$  can refine NbC, especially the interface relationship between them, has not been reported before.

Due to the ability of simulating and analyzing the interface properties and relationships of various phases in materials, the first principles calculation based on density functional theory (DFT) has aroused extensive attention [19-21]. Z.J. Liu et al. [19] researched work of adhesion and interfacial energy, etc. of Cu/Diamond interface by DFT calculation, which reveals the special viscous transfer phenomena of Cu/Diamond interface has a contribution to the different tribological properties. Y.X. Xu et al. [20] investigated the influence of different modulation ratios on TiAlN/TiN and TiAlN/ZrN multilayer interface structures, which show that the results of the calculations are consistent with the experimental results and the defects in the non-equilibrium deposition process are attributed to the formation of the metastable coherent interface. Our previous research shows that  $Y_2O_3$  can act as the heterogeneous nucleus of TiC and refine it, when Ti and  $Y_2O_3$  are added to Fe-based alloy simultaneously [21]. However, the interface relationship between  $YAlO_3$  and NbC has not been researched or reported by the first principles calculation at present.

In this research, the heterogeneous nucleation mechanism between  $YAlO_3$  and NbC is investigated by first principles calculation and experiment. Firstly, the electronic structure, stability and bonds characteristics of  $YAlO_3$ /NbC interface were calculated by the first

principles method and the possibility of YAlO<sub>3</sub> act as the heterogeneous nucleus of NbC was analyzed theoretically. Then, the microstructure and interface combination status of YAlO<sub>3</sub> and NbC in Fe-based alloy were observed by transmission electron microscope (TEM), which can provide experimental evidence for the analysis of YAlO<sub>3</sub> acting as the heterogeneous nucleus of NbC.

## 2. Computational details and experimental method

### 2.1. Calculation models

The crystal structure diagrams of YAlO<sub>3</sub> and NbC models used in the first principles calculation are shown in Fig.1. As shown in Fig.1, the bulk crystal models are YAlO<sub>3</sub> crystal unit cell with the orthorhombically distorted perovskite structure [22] and NbC crystal unit cell with the cubically NaCl structure [23]. Fig. 1(a) is YAlO<sub>3</sub> model and the optimized lattice constants are a=b=3.49 Å, c=11.43 Å. Fig. 1(b) is NbC model and the optimized lattice constants are a=b=c=4.48 Å.

### 2.2. Calculation methods

All the first principles calculations based on density functional theory (DFT) were performed by using the vienna ab-initio simulation package (VASP) [24,25]. The interactions between electron ions were treated by the method of projector-augmented wave theory [26,27]. The generalized gradient approximation method (GGA), which is parameterized by perdue, burke and ernzerhof (PBE), was used to describe exchange-correlation energy [28]. In all calculations of YAlO<sub>3</sub> and NbC, the cut-off energy [29] was set to 500 eV. K-points sampling grids, which plays a role of sampling in reduced brillouin zone, was acquired by Monkhorst-Pack method [21]. K-points for the bulk, surface and interface models were set as 8 x 8 x 8, 8 x 8 x 1 and 8 x 4 x 1. The thickness of vacuum layer in the surface and interface model was 10 Å. Broyden Fletcher Goldfarb Shannon(BFGS) algorithm was used to relax the models to optimize the structures. The energy changes in the structural optimization process converge to 1.0 x 10<sup>-5</sup> eV/atom and the maximum stress converges to 0.01 eV/Å.

### 2.3. Experiment methods

The Fe-based alloy with Y<sub>2</sub>O<sub>3</sub> and Nb additives was prepared by surfacing welding method, whose composition is as follows: Fe-27Cr-5.5C-0.5Nb-0.5Y<sub>2</sub>O<sub>3</sub> (wt%). The microstructure of the Fe based alloy was observed by JEM-2010 transmission electron microscope (TEM).

## 3. Results and analysis

### 3.1. Two-dimensional lattice mismatch.

The equation of two-dimensional lattice mismatch is as follows [30]:

$$\delta_{(hkl)_n}^{(hkl)_s} = \sum_{i=1}^3 \left[ \left( \left| d_{[uvw]_s}^i \cos\theta - d_{[uvw]_n}^i \right| / d_{[uvw]_n}^i \right) / 3 \right] \times 100\% \quad (1)$$

where (hkl)<sub>s</sub> is a low-index lattice plane of nucleation substrate; (hkl)<sub>n</sub> is a low-index lattice plane of nucleating phase; [uvw]<sub>s</sub> is a low-index crystal orientation in (hkl)<sub>s</sub>; [uvw]<sub>n</sub> is a low-index crystal orientation in (hkl)<sub>n</sub>; d<sub>[uvw]<sub>s</sub></sub> is the interatomic spacing along [uvw]<sub>s</sub>; d<sub>[uvw]<sub>n</sub></sub> is the interatomic spacing along [uvw]<sub>n</sub>; q is the angle between the [uvw]<sub>s</sub> and [uvw]<sub>n</sub>.

According to the Bramfitt two-dimensional lattice mismatch theory [30], substrate phase can

be very effective heterogeneous nucleus of nucleating phase when the lattice mismatch between them is smaller than 6%; substrate phase can be medium effective heterogeneous nucleus of nucleating phase when the lattice mismatch between them is in the range from 6% to 12%; and substrate phase cannot be effective heterogeneous nucleus of nucleating phase when the lattice mismatch between them is larger than 12%.

On the basis of the lattice optimization, the lattice mismatch of  $\text{YAlO}_3/\text{NbC}$  interface was calculated, which is listed in Table 1. The lattice mismatch of  $\text{YAlO}_3(001)/\text{NbC}(100)$  interface is 5.4%, which indicates that  $\text{YAlO}_3$  meets the geometric condition of being an effective heterogeneous nucleus of NbC. Therefore, the  $\text{YAlO}_3(001)$  slabs and NbC (100) slabs were selected to build surface and interface models.

## 3.2. Bulk property

### 3.2.1. Bulk property of $\text{YAlO}_3$

The bulk properties of  $\text{YAlO}_3$  are shown in Fig. 2 and the Fermi level is indicated by dashed line. Fig. 2(a) is the band structure of  $\text{YAlO}_3$ , which indicates that  $\text{YAlO}_3$  is an indirect bandgap semiconductor with a 2.82 eV band gap between the valence band and the conduction band (the valence band top and conduction band bottom are misaligned). Fig. 2(b) is the density of states (DOS) and the partial density of states (PDOS) of  $\text{YAlO}_3$ , which illustrates that the chemical bond of  $\text{YAlO}_3$  bulk structure is a mixture of ionic bonds and covalent ones. In the range of -6 eV to Fermi level, the major part of total DOS is the contribution of O-p orbit and Y atom has very little contribution, which reveals that ionic bond formed between the O atom and Y atom. The electrons transfer to the around of electronegative O atom. From -6 eV to -4.5 eV, the peak shape and the peak strength of Al-s orbit are similar to that of O-p orbit. From -4.5 eV to 3 eV, the peak shape and the peak strength of Al-p orbit are similar to that of O-p orbit, which indicates that there is resonance and orbital hybridization between the sp orbitals of Al atom and p orbit of O atom. Therefore, covalent bond formed between Al atom and O atom.

The calculated elastic moduli of  $\text{YAlO}_3$  is listed in Table 2. Based on the calculated elastic moduli, the Young's modulus, linear compressibility, shear modulus and Poisson's ratio calculated by the software of Gaillac et al. [31] are listed in Table 3. The maximum value of calculated Young's modulus of bulk  $\text{YAlO}_3$  is 263.02 GPa and the minimum value is 158.30 GPa. The maximum value of calculated linear compressibility of bulk  $\text{YAlO}_3$  is  $2.23 \text{ TPa}^{-1}$  and the minimum value is  $1.32 \text{ TPa}^{-1}$ . The maximum value of calculated shear modulus is 129.01 GPa and the minimum value is 57.25 GPa. The maximum value of calculated Poisson's ratio is 0.58 and the minimum value is -0.09. The Poisson's ratio of  $\text{YAlO}_3$  is negative, which indicates that it has similar properties with auxetic materials in some conditions.

The 3D and 2D views of Young's modulus, linear compressibility, shear modulus and Poisson's ratio of bulk  $\text{YAlO}_3$  are shown in Fig. 3. It can be known from Fig. 3(a) that the anisotropy of Young's modulus of bulk  $\text{YAlO}_3$  is large in x, y and z orientations. In Fig. 3(b), the anisotropy of linear compressibility of bulk  $\text{YAlO}_3$  is mainly the contribution of z orientation and there is no anisotropy in xy orientation. In Fig. 3(c), the anisotropy of shear modulus is very large. In Fig. 3(d), the anisotropy of Poisson's ratio of bulk  $\text{YAlO}_3$  is relatively complex and the negative value in xy plane indicates the bulk  $\text{YAlO}_3$  presents properties like auxetic materials in (110) orientation.

### 3.2.2. Bulk property of NbC

The bulk properties of NbC are shown in Fig. 4 and the Fermi level is indicated by dashed line.

Fig. 4(a) is the band structure of NbC and there are bands across the Fermi level, which indicates that the valence electrons can enter the conduction band through the Fermi surface. Therefore, NbC has some metallic characteristics. Fig. 4(b) is the DOS and PDOS of NbC, which illustrates that the chemical bond of NbC bulk structure is a mixture of covalent bonds and metallic ones. The DOS and PDOS of Nb atom have peaks at the Fermi level and the major part of them is the contribution of Nbd orbit, which indicates that NbC has some metallic bonds. From -7.5 eV to -2 eV, the peak shape and the peak strength of Nbd orbit are similar to that of C-p orbit, which indicates that there is resonance and orbital hybridization between the d orbits of Nb atom and p orbit of C atom. Therefore, covalent bond formed between Nb atom and C atom.

The calculated elastic moduli of NbC is listed in Table 4. Based on the calculated elastic moduli, the Young's modulus, linear compressibility, shear modulus and Poisson's ratio calculated by the software of Gaillac et al. [31] are listed in Table 5. The maximum value of calculated Young's modulus of NbC is 648.79 GPa and the minimum value is 440.97 GPa. The maximum value of calculated linear compressibility of NbC is 1.09 TPa<sup>-1</sup> and equal to the maximum value. The maximum value of calculated shear modulus of NbC is 282.96 GPa and the minimum value is 175.03 GPa. The maximum value of calculated Poisson's ratio of NbC is 0.369 and the minimum value is 0.108.

The 3D and 2D views of Young's modulus, linear compressibility, shear modulus and Poisson's ratio of NbC are shown in Fig. 5. It can be known from Fig. 5(a), the anisotropy of the Young's modulus of NbC is identical in x, y and z orientations. In Fig. 5(b), it is obvious that there is no anisotropy of the linear compressibility of NbC. From Fig. 5(c) and (d), it can be revealed that the anisotropy of the shear modulus of NbC is identical in x, y and z orientations and so does the Poisson's ratio. Therefore, we can reach the conclusion that the Young's modulus, linear compressibility, shear modulus and Poisson's ratio of NbC all have high symmetry. The mechanical properties of NbC are similar in the specific symmetrical crystal orientations. Especially the linear compressibility of NbC, it is same in every orientation, which indicates the absence of anisotropy.

### 3.3. Surface convergence test

Before building the interface models, surface convergence tests of YAlO<sub>3</sub> and NbC slabs were performed to determine the smallest atomic layers as well as to achieve the bulk properties. A 10 Å vacuum layer was adopted in surface and interface models to neutralize the interaction of the terminal atoms. In order to eliminate the dipole effect, all surface models have the same termination condition on the two terminal surfaces.

The surface models of NbC and YAlO<sub>3</sub> are shown in Fig. 6. Fig. 6(a) is NbC(100) surface model and the type of it is nonpolar surface, in which the number of Nb atom and C atom is same in each layer. Fig. 6(b) ~ (e) are the surface models of YAlO<sub>3</sub>(001) with four different termination conditions, and they are Y-terminated YAlO<sub>3</sub>(001) surface (b), O1-terminated one (c), O2-terminated one (d) and AlO-terminated one, respectively (e). All YAlO<sub>3</sub>(001) models are polar surfaces.

#### 3.3.1. Surface energy of NbC

The surface energy is one of the methods to prove that the surface model achieves the bulk-like properties with the increase of atomic layer number. The surface energy of NbC(110) model can be calculated by the Botteger Eqs [32]:

$$\sigma_{NbC(100)} = \frac{1}{2A} (E_{slab}^N - N\Delta E) \quad (2)$$

$$\Delta E = (E_{slab}^N - E_{slab}^{N-2})/2 \quad (3)$$

where  $\sigma_{NbC(100)}$  is the surface energy of NbC(100) model;  $E_{slab}^N$  slab and  $E_{slab}^{N-2}$  are the total energy of surface models with N and N-2 atomic layers respectively; A is the surface area of NbC(100) surface model. The surface energy of NbC(100) model with different atomic layer is listed in Table 6. When the layer number of the surface model reaches 13, NbC(100) surface energy is converged to 1.46 J/ m<sup>2</sup> commendably. It indicates that 13-layered NbC(100) model can achieve convergence and the bulk-like properties.

### 3.3.2. Surface energy of YAlO<sub>3</sub>

All four type YAlO<sub>3</sub>(001) models are polar surface models, and the surface energy can be calculated by equation as follow:

$$\sigma_{YAlO_3(001)} = \frac{1}{2A} (E_{slab} - N_Y \mu_Y - N_{Al} \mu_{Al} - N_O \mu_O) \quad (4)$$

where  $\sigma_{YAlO_3(001)}$  is the surface energy of YAlO<sub>3</sub>(001) model; A is the surface area of the model;  $E_{slab}$  is the total energy of surface model;  $N_Y$ ,  $N_{Al}$  and  $N_O$  are the numbers of Y atom, Al atom and O atom in surface model respectively;  $\mu_Y$ ,  $\mu_{Al}$  and  $\mu_O$  are the chemical potentials of Y atom, Al atom and O atom respectively.

The YAlO<sub>3</sub> bulk unit energy  $\mu_{YAlO_3}^{bulk}$  can be calculated by equation as follows:

$$\mu_{YAlO_3}^{bulk} = \mu_Y + \mu_{Al} + 3\mu_O \quad (5)$$

In YAlO<sub>3</sub>(001) Y-terminated surface model, the number of atoms satisfies the following equation:

$$N_Y = N_{Al} + 2 \quad N_O = 3N_{Al} \quad (6)$$

By combining equation (4), equation (5) and equation (6), the equation of the surface energy  $\sigma_{YAlO_3(001)}$  of YAlO<sub>3</sub>(001) Y-terminated model with only one variate  $\mu_Y$  is shown as follows:

$$\sigma_{YAlO_3(001)} = \frac{1}{2A} (E_{slab} - N_{Al} \mu_{YAlO_3}^{bulk} - 2\mu_Y) \quad (7)$$

In YAlO<sub>3</sub>(001) O1-terminated surface model, the number of atoms satisfies the following equation:

$$N_{Al} = N_Y - 2 \quad N_O = 3N_Y - 2 \quad (8)$$

By combining equation (4), equation (5) and equation (8), the equation of the surface energy  $\sigma_{YAlO_3(001)}$  of YAlO<sub>3</sub>(001) O1-terminated model can be simplified as follows:

$$\sigma_{YAlO_3(001)} = \frac{1}{2A} [E_{slab} - N_Y \mu_{YAlO_3}^{bulk} + 2(\mu_{Al} + \mu_O)] \quad (9)$$

In YAlO<sub>3</sub>(001) O2-terminated surface model, the number of atoms satisfies the following equation:

$$N_Y = N_{Al} - 2 \quad N_O = 3N_{Al} \quad (10)$$

By combining equation (4), equation (5) and equation (10), the equation of the surface energy  $\sigma_{YAlO_3(001)}$  of YAlO<sub>3</sub>(001) O2-terminated model can be simplified as follows:

$$\sigma_{YAlO_3(001)} = \frac{1}{2A} (E_{slab} - N_{Al} \mu_{YAlO_3}^{bulk} + 2\mu_Y) \quad (11)$$

In YAlO<sub>3</sub>(001) AlO-terminated surface model, the number of atoms satisfies the following equation:

$$N_{Al} = N_Y + 2 \quad N_O = 3N_Y + 2 \quad (12)$$

By combining equation (4), equation (5) and equation (12), the equation of the surface energy

$\sigma_{\text{YAlO}_3(001)}$  of  $\text{YAlO}_3(001)$  AlO-terminated model can be simplified as follows:

$$\sigma_{\text{YAlO}_3(001)} = \frac{1}{2A} \left[ E_{\text{slab}} - N_Y \mu_{\text{YAlO}_3}^{\text{bulk}} - 2(\mu_{\text{Al}} + \mu_{\text{O}}) \right] \quad (13)$$

The calculated chemical potentials of Y atom, Al atom and O atom at 0K and atmospheric pressure are  $\mu_{\text{Y}}=-6.43$  eV,  $\mu_{\text{Al}}=-3.74$  eV and  $\mu_{\text{O}}=-4.78$  eV respectively. The calculated chemical potential of each element is put into equation (7), equation (9), equation (11) and equation (13) to obtain the surface energy of the  $\text{YAlO}_3(001)$  surface models with different termination types.

The surface energies of 7-31 layers  $\text{YAlO}_3(001)$  O1-terminated models are listed in Table 7. When the layer of  $\text{YAlO}_3(001)$  O1-terminated model attains 23, the surface energy can converge to about  $6.37 \text{ J/m}^2$ . The surface energies of 7-31 layers  $\text{YAlO}_3(001)$  O2-terminated models are listed in Table 8. When the layer of  $\text{YAlO}_3(001)$  O2-terminated model attains 19, the surface energy can converge to about  $11.22 \text{ J/m}^2$ . The surface energies of 5e25 layers  $\text{YAlO}_3(001)$  Y-terminated models are listed in Table 9. When the layer of  $\text{YAlO}_3(001)$  Y-terminated model attains 21, the surface energy can converge to about  $2.07 \text{ J/m}^2$ . The surface energies of  $\text{YAlO}_3(001)$  AlO-terminated models are negative values, which indicate these models are unstable or in a metastable state. Therefore, this type model is not taken into account in the following researches.

According to the results of surface convergence tests, which can be confirmed is that 13 layered NbC(100) surface model, 23 layered  $\text{YAlO}_3(001)$  O1-terminated surface model, 19 layered  $\text{YAlO}_3(001)$  O2-terminated surface model and 21 layered  $\text{YAlO}_3(001)$  Y-terminated one can be used to build interface models.

### 3.4. Interfacial property

Based on the results of two-dimensional lattice mismatch and surface convergence tests, six interface structures were constructed with consideration of different stacking modes. The schematically structures of different interface models are shown in Fig. 7. As shown in Fig. 7, six interface structures were named according to the interfacial atoms corresponding situation: Fig. 7(a) Nb-Y, (b) CY, (c) Nb-O1, (d) C-O1, (e) Nb-O2 and (f) C-O2.

#### 3.4.1. Work of adhesion and interfacial energy

The interfacial work of adhesion and interfacial energy are closely related to the interfacial electronic structures and bond characters, which can be used to evaluate the bonding strength and stability of the interface system. The work of adhesion can be defined as the reversible work required in separating an interface into two free surfaces, which can determine the bonding strength of the interface structure. The interfacial work of adhesion can be calculated by the equation as follows [33]:

$$W_{\text{ad}} = \frac{1}{A} \left( E_{\text{YAlO}_3=\text{NbC}} - E_{\text{YAlO}_3} - E_{\text{NbC}} \right) \quad (14)$$

where  $E_{\text{YAlO}_3=\text{NbC}}$  is the total energy of the interface structure;  $E_{\text{YAlO}_3}$  and  $E_{\text{NbC}}$  are the total energy of isolated  $\text{YAlO}_3(001)$  and NbC(100) surface models; A is the interface area. The interfacial energy is an important parameter to evaluate the interface stability. Generally, the smaller the interfacial energy is, the interface structure is more stable [21]. The interfacial energy can be calculated by the equation as follows [34]:

$$\gamma = \sigma_{\text{YAlO}_3} + \sigma_{\text{NbC}} - W_{\text{ad}} \quad (15)$$

where  $\sigma_{\text{YAlO}_3}$  and  $\sigma_{\text{NbC}}$  are the surface energy of  $\text{YAlO}_3(001)$  and  $\text{NbC}(100)$  models;  $W_{\text{ad}}$  is the work of adhesion of  $\text{YAlO}_3(001)/\text{NbC}(100)$  interface.

The  $W_{\text{ad}}$  of  $\text{YAlO}_3(001)/\text{NbC}(100)$  interface model is listed in Table 10. It can be concluded that the  $W_{\text{ad}}$  of different interfaces has the following relationship:  $W_{\text{ad}}(\text{C-O2}) > W_{\text{ad}}(\text{Nb-O2}) > W_{\text{ad}}(\text{C-Y}) > W_{\text{ad}}(\text{Nb-Y}) > W_{\text{ad}}(\text{Nb-O1}) > W_{\text{ad}}(\text{C-O1})$ . The  $\gamma$  of  $\text{YAlO}_3(001)/\text{NbC}(100)$  interface model is listed in Table 11. It can be concluded that the  $\gamma$  of different interfaces has the following relationship:  $\gamma(\text{C-Y}) < \gamma(\text{Nb-Y}) < \gamma(\text{C-O2}) < \gamma(\text{Nb-O2}) < \gamma(\text{Nb-O1}) < \gamma(\text{C-O1})$ . According to the results of the  $W_{\text{ad}}$  and  $\gamma$ , it can be derived that C-O2 interface has the strongest binding force and C-Y interface has the best stability. In order to further analyze the properties of the interfaces, the electronic structure of C-O2, Nb-O2, C-Y and Nb-Y interfaces were calculated. The  $W_{\text{ad}}$  and  $\gamma$  of Nb-O1 and C-O1 interfaces are both inferior, so they are not taken into account in the following researches.

### 3.4.2. Interface electronic structure and bond characteristics

The charge density difference can be used to analyze the transfer of interatomic charge, and the charge accumulation regions and charge depletion regions are ascertained. The charge density difference can be calculated by the equation as follows [35]:

$$\rho_d = \rho_{\text{total}} - \rho_{\text{YAlO}_3} - \rho_{\text{NbC}} \quad (16)$$

where  $\rho_{\text{total}}$  is the total charge density of the interface system;  $\rho_{\text{YAlO}_3}$  and  $\rho_{\text{NbC}}$  are the charge density of isolated  $\text{YAlO}_3$  slab and  $\text{NbC}$  slab in the same interface structure.

The characterization of localized distribution characteristics of electrons can be performed by electron localization function (ELF), which can also confirm the bond-types. The ELF can be calculated by the equation as follows [36]:

$$\text{ELF} = 1 / \left[ 1 + \left( \frac{D_{(r)}}{Dh_{(r)}} \right)^2 \right] \quad (17)$$

where  $D_{(r)}$  is the real electron gas density;  $Dh_{(r)}$  is the uniform electron gas density. ELF values are between 0 and 1. With the upper limit  $\text{ELF} = 1$  corresponding to perfect localization and the value  $\text{ELF} = 1/2$  corresponding to electron gas-like pair probability. While the value  $\text{ELF} = 0$  means that electron might be entirely delocalized (or there is no electrons).

The charge density difference images of Nb-Y, C-Y, Nb-O2 and CO2 interfaces are shown in Fig. 8. In Fig. 8(a), there are charge depletion regions between the interfacial Nb atoms and the Y atoms and charge accumulation regions are away from the interface, which indicates that the electrons of Nb atoms and Y atoms near interface transferred away from the interface atoms during the interfacial bonding process. In Fig. 8(b), there are charge depletion regions between the interfacial C atoms and the Y atoms, which indicate that the electrons of C atoms and Y atoms near interface are transferred away from the interface atoms during the interfacial bonding process. In addition, the charge depletion region of Y atom is much larger than that of C atom, which reveals that Y atom loses more charge. In Fig. 8(c), there are charge sharing regions between the interfacial Nb atoms and O atoms. There are charge depletion regions on the side of the Nb atoms and there are obvious charge accumulation regions around the O atoms, which indicate that the electrons of Nb atoms are transferred to O atoms during the interfacial bonding process. In Fig. 8(d), there are charge sharing regions between the interfacial C atoms and O atoms. In addition, there are also charge depletion regions near the interfacial C atoms

and O atoms, which reveal that the electrons of C atoms and O atoms are transferred to the region between the two atoms during the interfacial bonding process. However, there are charge accumulation regions around the O atoms, which indicates that O atom is more electronegative than C atom and it is also easier to get electrons. Therefore, the charge sharing region between C atom and O atom is deflected to the O atom side.

The ELF images of Nb-Y, C-Y, Nb-O<sub>2</sub> and C-O<sub>2</sub> interfaces are shown in Fig. 9. In Fig. 9(a), the ELF value between interfacial Nb atom and Y atom is in the range of 0-0.3, which reveals the ionic bond and metallic bond formed between the two atoms. There is a region in the middle of the interface with ELF value about 0.5, which indicates the formation of a weaker covalent bond. In Fig. 9(b), the ELF value between interfacial C atom and Y atom is in the range of 0.3-0.5, which indicates the formation of a weaker covalent bond. In Fig. 9(c), the ELF value between interfacial Nb atom and O atom is approximately 0.5, which reveals the formation of covalent bond. In Fig. 9(d), the ELF value between interfacial C atom and O atom is in the range of 0.7-0.9, which indicates the formation of strong covalent bond.

The DOS and crystal orbit overlap population (COOP) images of Nb-Y, C-Y, Nb-O<sub>2</sub> and C-O<sub>2</sub> interfaces are shown in Fig. 10. In Fig. 10(a), the COOP between the Nb-Y interfacial C atom and Y atom is positive value in the range of -6 eV ~ -3 eV and -11.5 eV ~ -9 eV, which presents a bonding action and has a contribution to the formation of Nb-Y interfacial covalent bonds. The COOP between the Nb-Y interfacial Nb atom and Y atom is positive value near the Fermi level, which presents a bonding action. However, the COOP between the Nb-Y interfacial Nb atom and Y atom is negative value away from the Fermi level, which presents an antibonding action. Therefore, the Nb-Y interfacial Nb atoms and Y atoms have contributions to the formation of interfacial metallic bonds. In Fig. 10(b), the COOP between the C-Y interfacial C atom and Y atom is positive in the range of -6 eV to the Fermi level, which presents a bonding action and has a contribution to the formation of C-Y interfacial covalent bonds. The COOP between the C-Y interfacial Nb atom and Y atom is positive value near the Fermi level, which presents a bonding action. However, the COOP between the C-Y interfacial Nb atom and Y atom is negative value away from the Fermi level, which presents an antibonding action. Therefore, the C-Y interfacial Nb atoms and Y atoms have contributions to the formation of interfacial metallic bonds. In Fig. 10(c), the COOP between the Nb-O<sub>2</sub> interfacial Nb atom and O atom is positive in the range of -7 eV to -2 eV, which presents a bonding action. The COOP between the Nb-O<sub>2</sub> interfacial C atom and O atom is positive in the range of -4 eV to -2 eV, which presents a bonding action. The COOP between the Nb-O<sub>2</sub> interfacial Nb atom and O atom (C atom and O atom) is negative value away from the Fermi level, which presents an antibonding action. By comparing their COOP, it can be revealed that the chemical bond between Nb atom and O atom is stronger than that between C atom and O atom, and they all have contributions to the formation of interfacial covalent bond. In Fig. 10(d), the COOP between the Nb-O<sub>2</sub> interfacial C atom and O atom (Nb atom and O atom) is positive in the range of -8 eV to -6 eV, which presents a bonding action. Both of their COOPs are negative values in a large region near the Fermi level, which presents an antibonding action. By comparing their COOP values, it can be revealed that the chemical bond between C atom and O atom is stronger than that between Nb atom and O atom, and they all have contributions to the formation of interfacial covalent bond.

### 3.5. TEM observation of heterogeneous nucleation interface

The TEM images of YAlO<sub>3</sub> and NbC in the Fe-based surfacing alloy are shown in Fig. 11. Fig. 11(a) is the bright field image of the drop-shaped particle. The dark field images of its internal

square region and outer annulus region are shown in Fig. 11(b) and (c), and their selected area diffraction patterns (SADPs) are shown in the top right corner of Fig. 11(b) and (c). According to the analysis of SADPs, it can be confirmed that the internal square particle is  $\text{YAlO}_3$  and the outer annulus is NbC. It is obvious that NbC grows around  $\text{YAlO}_3$  and they are combined together tightly, which proves that  $\text{YAlO}_3$  can act as the heterogeneous nucleus of NbC experimentally.

#### 4. Discussion on the validity of heterogeneous nucleation

The two-dimensional lattice mismatch of  $\text{YAlO}_3(001)/\text{NbC}(100)$  interface is 5.4%, which indicates that  $\text{YAlO}_3$  can act as an effective heterogeneous nucleus of NbC and provides a geometric structure basis to explain the heterogeneous nucleation mechanism. On the basis of the lattice mismatch calculation, the work of adhesion and interfacial energy of  $\text{YAlO}_3(001)/\text{NbC}(100)$  interfaces were calculated by the first principles calculation. The work of adhesion of different interface models has the following relationship:  $W_{\text{ad}}(\text{C-O2}) > W_{\text{ad}}(\text{Nb-O2}) > W_{\text{ad}}(\text{C-Y}) > W_{\text{ad}}(\text{Nb-Y}) > W_{\text{ad}}(\text{Nb-O1}) > W_{\text{ad}}(\text{C-O1})$ . The interfacial energy of different interface models has the following relationship:  $\gamma(\text{C-Y}) < \gamma(\text{Nb-Y}) < \gamma(\text{C-O2}) < \gamma(\text{Nb-O2}) < \gamma(\text{Nb-O1}) < \gamma(\text{C-O1})$ . Although the work of adhesion of the C-O2 model is the largest, it can be seen from the interfacial charge density difference that there is a tremendous lattice distortion between interfacial C atom and O atom. Therefore, the stability of C-O2 is poor. Due to the large electronegativity of C atom and O atom, they will have a strong competition for electrons during the bonding process. However, O atoms are more electronegative than C atoms, which lead to the formation of a polar covalent bond and the unbalanced moment of force action. Therefore, there is a deflection of the chemical bond between C atom and O atom, which lead to the result that the interface structure distorted to the one with a very large lattice mismatch. The most stable interface is C-Y model with the smallest interfacial energy ( $\gamma(\text{CY}) = 0.54 \text{ J/m}^2$ ), which provides an energy condition as the theoretical basis for  $\text{YAlO}_3$  act as the heterogeneous nucleus of NbC. The experimental results show that NbC grows around  $\text{YAlO}_3$  and they are combined together tightly, which proved that  $\text{YAlO}_3$  can act as the effective heterogeneous nucleus of NbC experimentally.

#### 5. Conclusions

- (1) The two-dimensional lattice mismatch of  $\text{YAlO}_3(001)$  slab and  $\text{NbC}(100)$  slab is 5.4% (<6%), which indicates  $\text{YAlO}_3$  can act as the effective heterogeneous nucleus of NbC.
- (2) The chemical bond of  $\text{YAlO}_3$  bulk structure is a mixture of ionic bond and covalent bond. The chemical bond of NbC bulk structure is a mixture of covalent bond and metallic bond. The chemical bonds of Nb-Y interface and C-Y interface both are mixture of covalent bond and metallic bond. The chemical bonds of Nb-O2 interface and C-O2 interface both are covalent bonds. The interface structure with the best stability is C-Y model, which has the smallest interfacial energy ( $\gamma(\text{C-Y}) = 0.54 \text{ J/m}^2$ ) in the six interface models.
- (3) The results of TEM show that the internal square particle is  $\text{YAlO}_3$  and the outer annulus particle is NbC. NbC grows around  $\text{YAlO}_3$  and they are combined together tightly. Therefore,  $\text{YAlO}_3$  can act as the effective heterogeneous nucleus of NbC.

#### Acknowledgement

The authors would like to express their gratitude for projects supported by the National Natural Science Foundation of China (No. 51471148 and No.51771167), the Hebei province Basic Research Foundation of China (No. 16961008D).

## References

- [1] B. Vishwanadh, A. Arya, R. Tewari, G.K. Dey, Formation mechanism of stable NbC carbide phase in Nb-1Zr-0.1C (wt.%) alloy, *Acta Mater.* 144 (2018) 470-483.
- [2] W. Zeng, J.W. Xie, D.S. Zhou, Z.Q. Fu, D.L. Zhang, E.J. Lavernia, In-situ formation of NbC in nanocrystalline Cu, *J. Alloys Compd.* 725 (2017) 334-341.
- [3] A. Szczotok, K. Rodak, Microstructural studies of carbides in MAR-M247 nickel-based superalloy, *IOP Conf. Ser. Mater. Sci. Eng.* 35 (2012) 12006.
- [4] A.J. Craven, K. He, L.A.J. Garvie, T.N. Baker, Complex heterogeneous precipitation in Titanium-Niobium microalloyed Al-killed HSLA steels-I. (Ti,Nb)(C,N) particles, *Acta Mater.* 48 (2000) 3857-3868.
- [5] M. Woydt, H. Mohrbacher, The tribological and mechanical properties of niobium carbides (NbC) bonded with cobalt or Fe<sub>3</sub>Al, *Wear* 321 (2014) 1-7.
- [6] Z.Y. Zhang, X.J. Sun, Z.Q. Wang, Z.D. Li, Q.L. Yong, G.D. Wang, Carbide precipitation in austenite of NbMo-bearing low-carbon steel during stress relaxation, *Mater. Lett.* 159 (2015) 249-252.
- [7] S. Qin, B. Liao, L. Mao, F.R. Xiao, A novel method for preparing nano-NbC/Fe powder and nano-NbC particle reinforced cast low-carbon steel, *Mater. Lett.* 121 (2014) 162-165.
- [8] H.H. Zhang, H.H. Xiong, D.Z. Wang, W.L. Wang, Mechanism of NbC heterogeneous nucleation on TiN in microalloyed steel: a first-principles study, *Comput. Mater. Sci.* 146 (2018) 126-133.
- [9] S. Liu, Z.J. Wang, Z.J. Shi, Y.F. Zhou, Q.X. Yang, Experiments and calculations on refining mechanism of NbC on primary M<sub>7</sub>C<sub>3</sub> carbide in hypereutectic Fe-Cr-C alloy, *J. Alloys Compd.* 713 (2017) 108-118.
- [10] G.K. Tirumalasetty, M.A. van Huis, C.M. Fang, Q. Xu, F.D. Tichelaar, D.N. Hanlon, J. Sietsma, H.W. Zandbergen, Characterization of NbC and (Nb, Ti)N nanoprecipitates in TRIP assisted multiphase steels, *Acta Mater.* 59 (2011) 7406-7415.
- [11] D. Poddar, P. Cizek, H. Beladi, P.D. Hodgson, The evolution of microbands and their interaction with NbC precipitates during hot deformation of a Fe-30Ni-Nb model austenitic steel, *Acta Mater.* 99 (2015) 347-362.
- [12] K. Hamano, S. Ohta, Y. Ozaki, Effects of rare earth oxides on sintering of alumina, *Yogyo-Kyokai-Shi* 87 (1979) 632-641.
- [13] A.M. Thompson, K.K. Soni, H.M. Chan, M.P. Harmer, D.B. Williams, J.M. Chabala, R.L. Setti, Dopant distributions in rare-earth-doped alumina, *J. Am. Ceram. Soc.* 80 (1997) 373-376.
- [14] N.M. Khalil, M.B. Hassan, E.M.M. Ewais, F.A. Saleh, Sintering, mechanical and refractory properties of MA spinel prepared via co-precipitation and sol-gel techniques, *J. Alloys Compd.* 496 (2010) 600e607.
- [15] J. Yang, X.R. Hou, P. Zhang, Y.F. Zhou, Y.L. Yang, X.J. Ren, Q.X. Yang, Mechanical properties of the hypereutectoid Fe-Cr-C hardfacing coatings with different nano-Y<sub>2</sub>O<sub>3</sub> additives and the mechanism analysis, *Mater. Sci. Eng. A* 655(2016) 346-354.
- [16] S. Liu, J. Zhang, Z.J. Wang, Z.J. Shi, Y.F. Zhou, X.J. Ren, Q.X. Yang, Refinement and homogenization of M<sub>7</sub>C<sub>3</sub> carbide in hypereutectic Fe-Cr-C coating by Y<sub>2</sub>O<sub>3</sub> and TiC, *Mater. Char.* 132 (2017) 41-45.
- [17] J.S. Lee, Molten salt synthesis of YAlO<sub>3</sub> powders, *Mater. Sci. Pol.* 31 (2013) 240e245.
- [18] C.Q. Li, Z.H. Wang, M.F. Zhang, H.B. Zuo, Interactions between Y<sub>2</sub>O<sub>3</sub>-Al mixture studied by solid-state reaction method, *Vacuum* 87 (2013) 7-10.
- [19] Z.J. Liu, S.X. Zheng, Z.B. Lu, J.B. Pu, G.G. Zhang, Adhesive transfer at copper/diamond interface and adhesion reduction mechanism with fluorine passivation: a first-principles study, *Carbon* 127 (2018) 548-556.
- [20] Y.X. Xu, L. Chen, F. Pei, K.K. Chang, Y. Du, Effect of the modulation ratio on the

- interface structure of TiAlN/TiN and TiAlN/ZrN multilayers: first-principles and experimental investigations, *Acta Mater.* 130 (2017) 281-288.
- [21] Z.J. Shi, S. Liu, Y.K. Gao, Y.F. Zhou, X.L. Xing, X.J. Ren, Q.X. Yang, Mechanism of Y<sub>2</sub>O<sub>3</sub> as heterogeneous nucleus of TiC in hypereutectic Fe-Cr-C-Ti-Y<sub>2</sub>O<sub>3</sub> coating: first principles calculation and experiment research, *Mater. Today Commun.* 13 (2017) 80-91.
- [22] E.F. Bertaut, J. Mareschal, Un nouveau type de structure hexagonale: Al<sub>2</sub>O<sub>3</sub>, *C. R. Acad. Sci.* 275 (1963) 867-870.
- [23] J.H. Jang, C.H. Lee, Y.U. Heo, D.W. Suh, Stability of (Ti,M)C (M= Nb, V, Mo and W) carbide in steels using first-principles calculations, *Acta Mater.* 60 (2012)208-217.
- [24] G. Kresse, J. Furthmüller, Efficient iterative schemes for ab initio total-energy calculations using a plane-wave basis set, *Phys. Rev. B* 54 (1996) 11169-11186.
- [25] G. Kresse, J. Furthmüller, Efficiency of ab-initio total energy calculations for metals and semiconductors using a plane-wave basis set, *Comput. Mater. Sci.*6 (1996) 15-50.
- [26] P.E. Blochl, Projector augmented-wave method, *Phys. Rev. B* 50 (1994)17953-17979.
- [27] G. Kresse, D. Joubert, From ultrasoft pseudopotentials to the projector augmented wave method, *Phys. Rev. B* 59 (1999) 1758-1775.
- [28] J.P. Perdew, K. Burke, M. Ernzerhof, Generalized gradient approximation made simple, *Phys. Rev. Lett.* 77 (1996) 3865-3868.
- [29] N. Troullier, J.L. Martins, Efficient pseudopotentials for plane-wave calculations, *Phys. Rev. B* 43 (1991) 1993-2006.
- [30] B.L. Bramfitt, The effect of carbide and nitride additions on the heterogeneous nucleation behavior of liquid iron, *Metall. Trans.* 1 (1969) 1978-1995.
- [31] R. Gaillac, P. Pullumbi, F.X. Coudert, ELATE: an open-source online application for analysis and visualization of elastic tensors, *J. Phys. Condens. Matter* 28 (2016), 275201.
- [32] J. Boettger, Nonconvergence of surface energies obtained from thin-film calculations, *Phys. Rev. B* 49 (1994) 16798-16800.
- [33] Y.J. Xian, R.Z. Qiu, X. Wang, P.C. Zhang, Interfacial properties and electron structure of Al/B<sub>4</sub>C interface: a first-principle study, *J. Nucl. Mater.* 478 (2016) 227-235.
- [34] A. Ernst, G. van der Laan, W.M. Temmerman, S.S. Dhesi, Z. Szotek, Contesting results for magnetic moments in nickel thin films, *Phys. Rev. B* 62 (2000) 9543-9547.
- [35] V. Fiorentini, M. Methfessel, Extracting convergent surface energies from slab calculations, *J. Phys. Condens. Matter* 8 (1996) 6525-6529.
- [36] A.D. Becke, K.E. Edgecombe, A simple measure of electron localization in atomic and molecular systems, *J. Chem. Phys.* 92 (1990) 5397-5403.

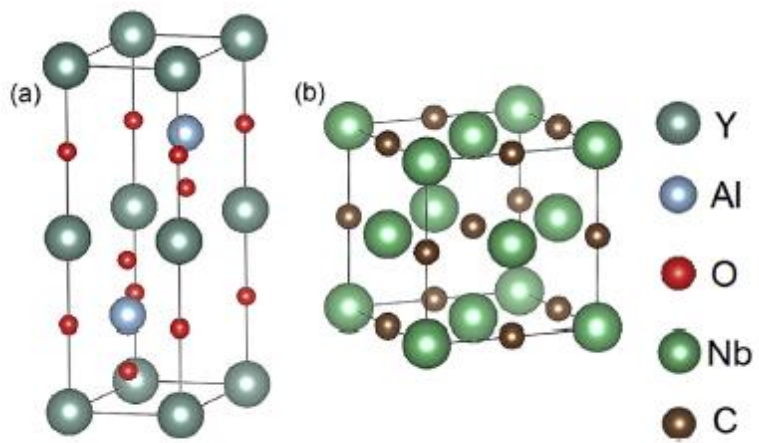


**Fig. 1.** Crystal structures used in calculation (a)  $YAlO_3$  and (b) NbC.

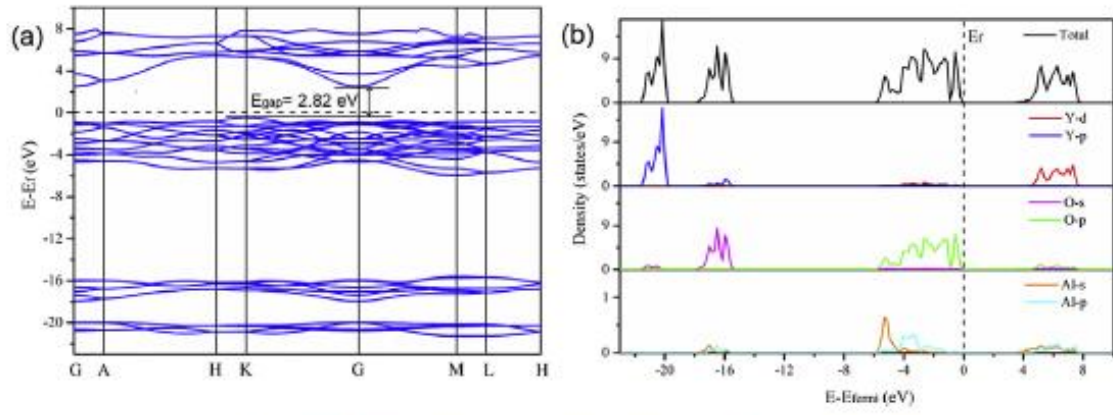


**Fig. 2.** Calculated band structure (a) and density of states(DOS) (b) of  $YAlO_3$ .

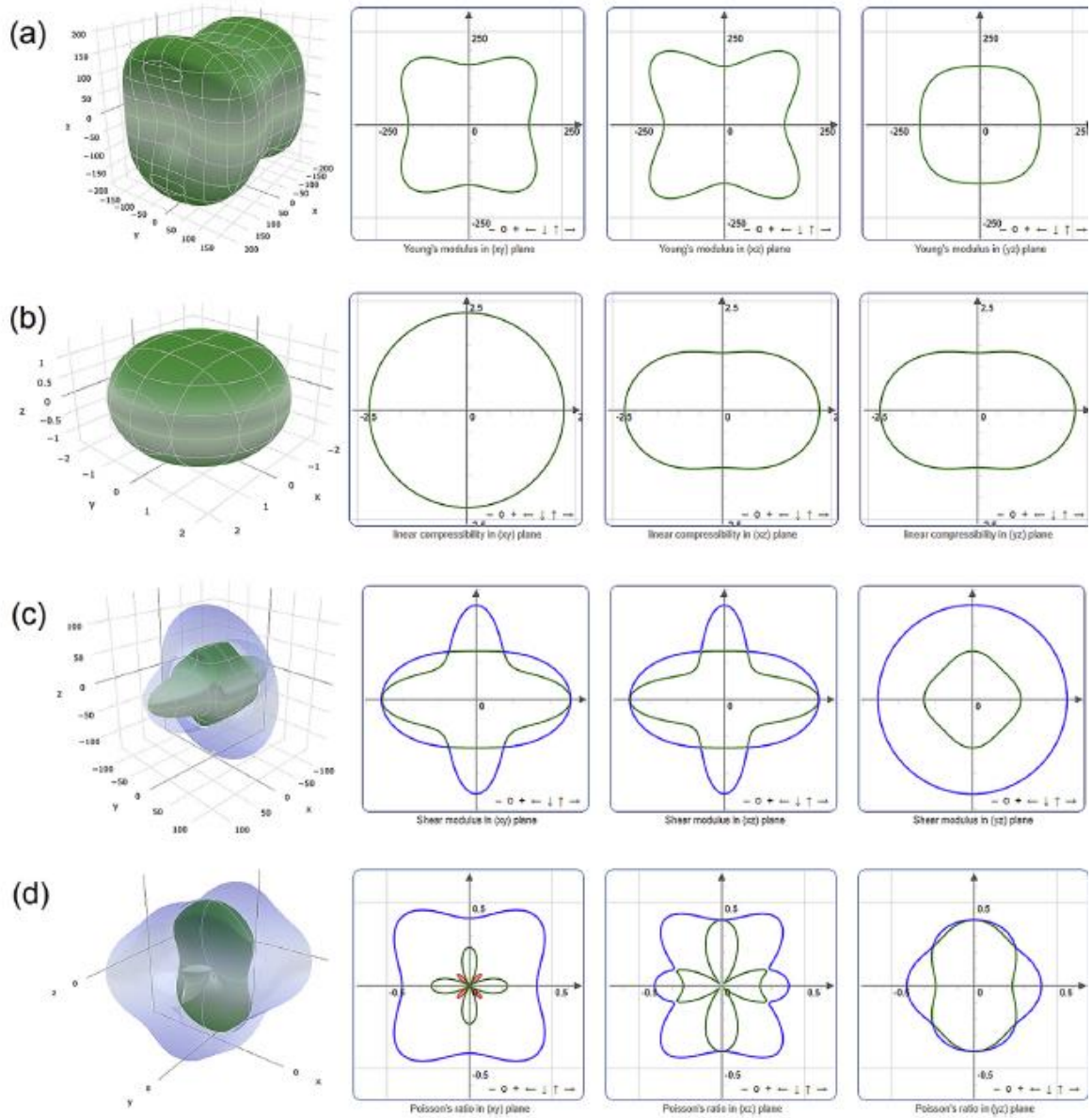


**Fig. 3.** 3D and 2D views for Young's modulus (a), Linear compressibility (b), Shear modulus (c) and Poisson's ratio (d) of YAIO<sub>3</sub> bulk.

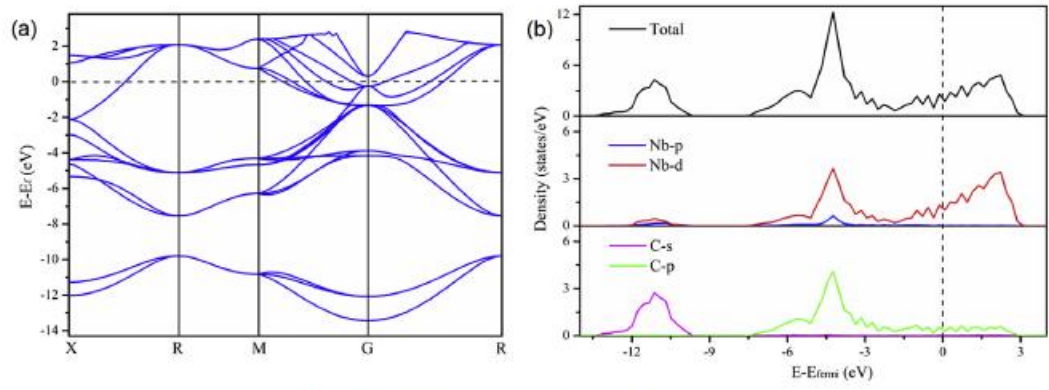


**Fig. 4.** Calculated band structure (a) and density of states (b) of NbC.

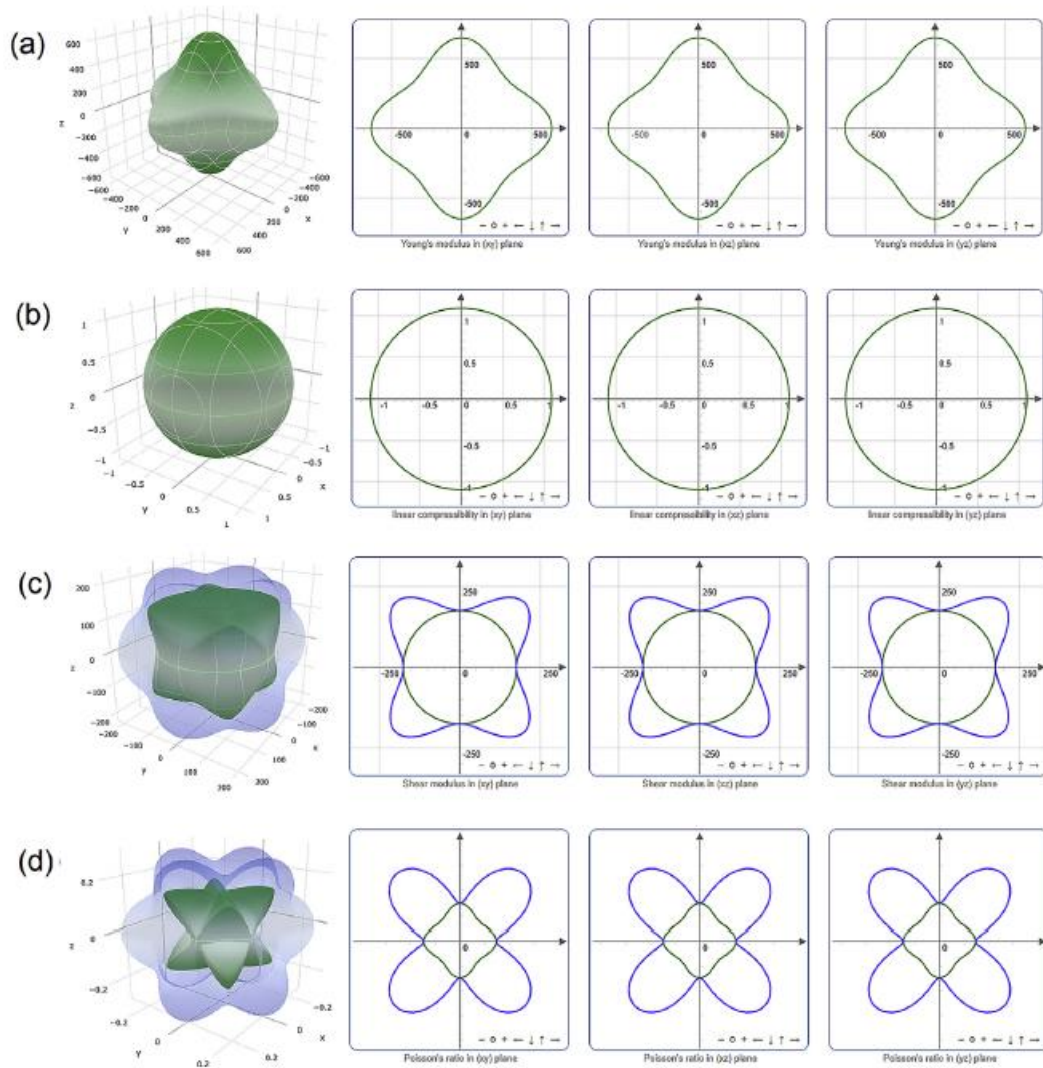


Fig. 5. The 3D and 2D views for Young's modulus (a), Linear compressibility (b), Shear modulus (c) and Poisson's ratio (d) of NbC bulk.

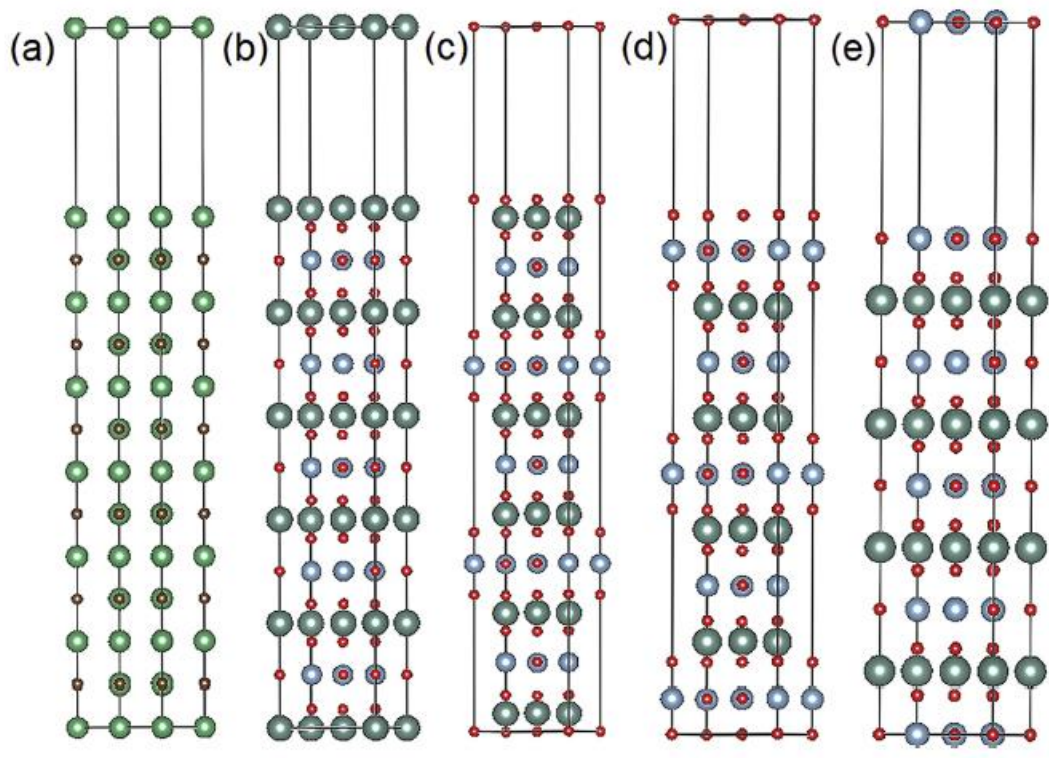
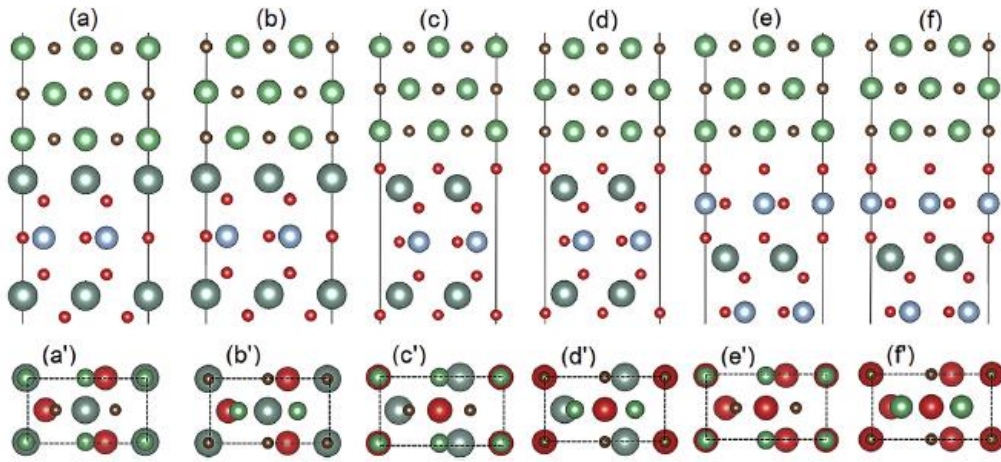


Fig. 6. Surface models of (a) NbC(100), (b)  $\text{YAlO}_3(001)$ -Y-terminated, (c) O1-terminated, (d) O2-terminated, (e) AlO-terminated.



**Fig. 7.** Schematically structures of interface models. (a) Nb-Y, (b) C-Y, (c) Nb-O1, (d) C-O1, (e) Nb-O2, (f) C-O2 and (a')-(f') top views of the interface models, respectively.

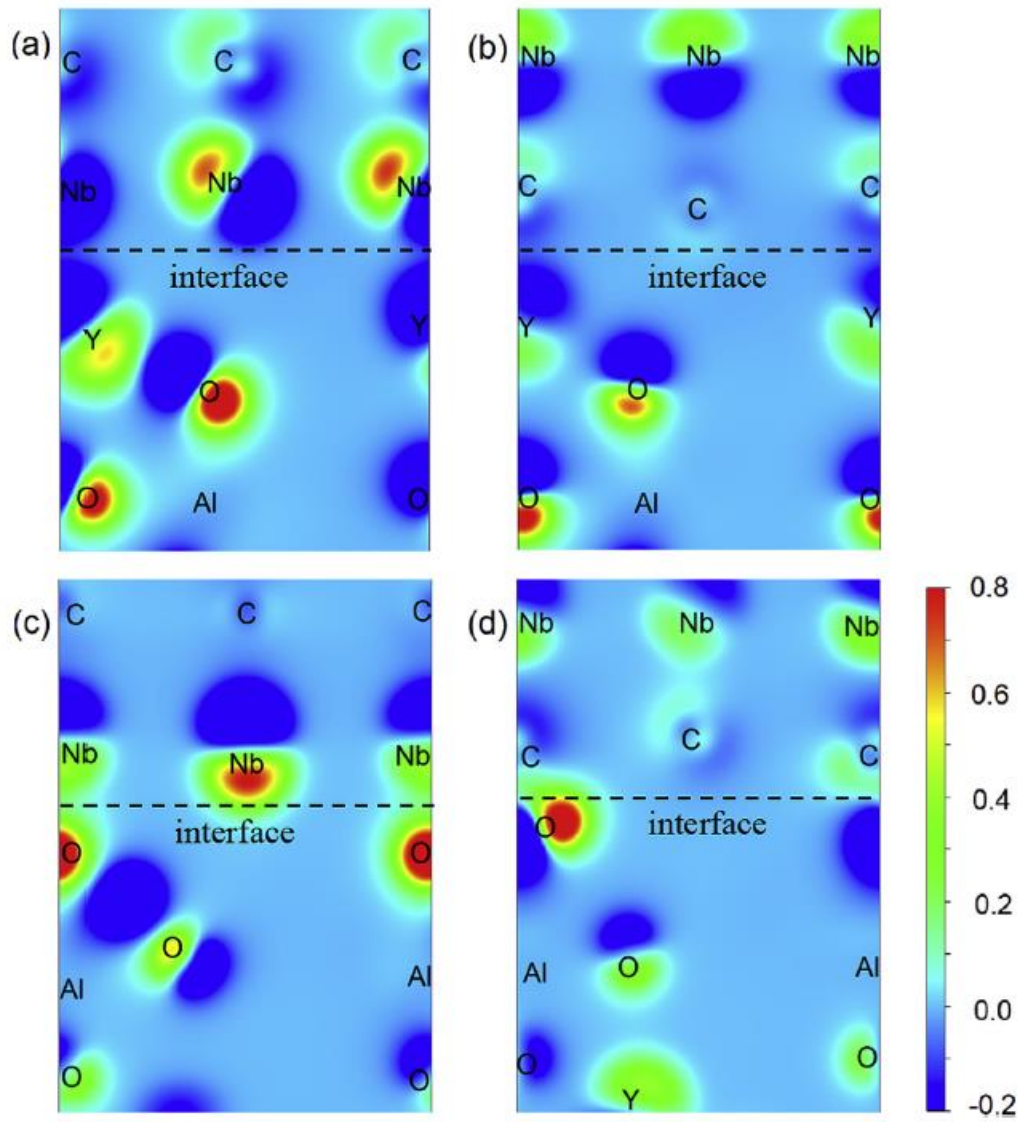


Fig. 8. Charge density difference of the (001) slice of  $\text{YAlO}_3/\text{NbC}$  interfaces. (a) Nb-Y, (b) C-Y, (c) Nb-O<sub>2</sub>, (d) C-O<sub>2</sub>.

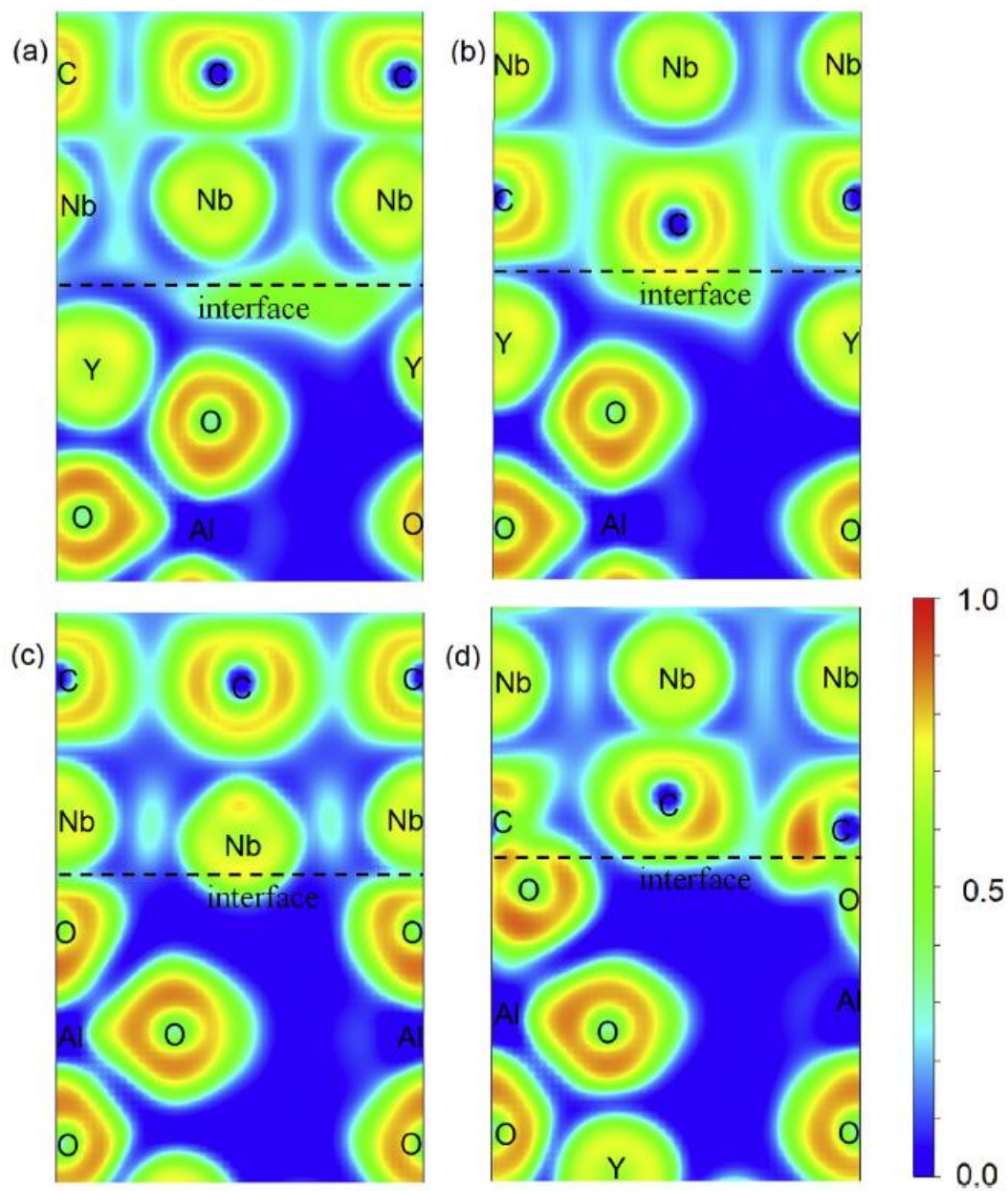
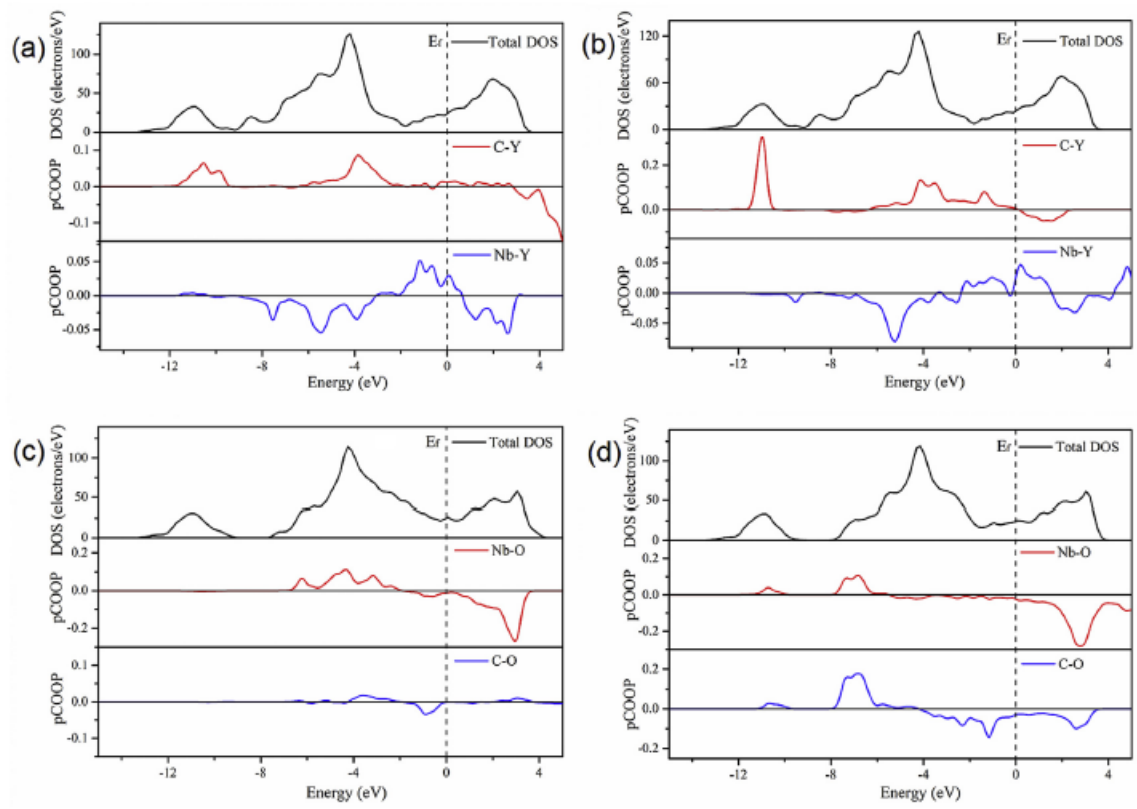


Fig. 9. ELF maps of the (001) slice of  $\text{YAlO}_3/\text{NbC}$  interfaces. (a) Nb-Y, (b) C-Y, (c) Nb-O2, (d) C-O2.



**Fig. 10.** DOS and partial-COOP of YAlO<sub>3</sub>/NbC interfaces. (a) Nb-Y, (b) C-Y, (c) Nb-O<sub>2</sub>, (d) C-O<sub>2</sub>.

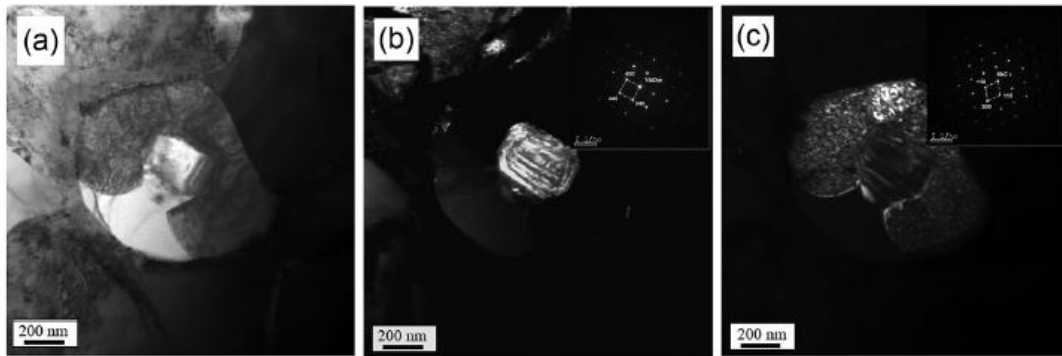


Fig. 11. TEM images of Fe-based surfacing alloy, (a) bright field image of the drop-shaped particle, dark field images and SADPs of the core (b) and annulus (c).

**Table 1**Calculated lattice mismatch between  $Y_2O_3$  and NbC.

Matching face	$YAlO_3(001)//NbC(100)$			$YAlO_3(001)//NbC(110)$			$YAlO_3(001)//NbC(111)$		
	[0 $\bar{1}$ 0]	[210]	[100]	[0 $\bar{1}$ 0]	[210]	[100]	[0 $\bar{1}$ 0]	[210]	[100]
[uvw] $YAlO_3$	[0 $\bar{1}$ 0]	[210]	[100]	[0 $\bar{1}$ 0]	[210]	[100]	[0 $\bar{1}$ 0]	[210]	[100]
[uvw]NbC	[0 $\bar{1}$ 1]	[011]	[010]	[001]	[1 $\bar{1}$ 0]	[1 $\bar{1}$ 1]	[1 $\bar{1}$ 0]	[11 $\bar{2}$ ]	[10 $\bar{1}$ ]
$\theta(^{\circ})$	0	0	3.435	0	0	5.264	0	0	0
$dYAlO_3(\text{\AA})$	6.051	3.493	6.987	6.051	3.493	6.987	6.051	3.493	6.987
$dNbC(\text{\AA})$	6.339	3.169	7.087	6.339	4.482	7.764	5.490	3.169	6.339
$\delta(\%)$	5.4			12.3			10.2		

**Table 2**Calculated elastic moduli of  $YAlO_3$ .

Total elastic moduli (kBar)							
Direction	XX	YY	ZZ	XY	YZ	ZX	
XX	2474.9817	1153.3626	1435.7516	-0.0000	-0.0000	0.0000	0.0000
YY	1153.3626	2474.9817	1435.7516	0.0000	0.0000	-0.0000	-0.0000
ZZ	1435.7516	1435.7516	2719.2276	-0.0000	-0.0000	0.0000	0.0000
XY	-0.0000	0.0000	-0.0000	660.8095	-0.0000	-0.0000	-0.0000
YZ	-0.0000	0.0000	-0.0000	-0.0000	1290.0517	-0.0000	-0.0000
ZX	0.0000	-0.0000	0.0000	0.0000	-0.0000	1290.0517	1290.0517

**Table 3**Young's modulus, linear compressibility, shear modulus and Poisson's ratio of  $YAlO_3$ .

$YAlO_3$	Young's modulus GPa		Linear compressibility $TPa^{-1}$		Shear modulus GPa		Poisson's ratio	
	$E_{min}$	$E_{max}$	$\beta_{min}$	$\beta_{max}$	$G_{min}$	$G_{max}$	$\nu_{min}$	$\nu_{max}$
Value	158.30	263.02	1.32	2.23	57.25	129.01	-0.09	0.58
Anisotropy	1.662		1.695		2.253		$\infty$	

**Table 4**

Calculated elastic moduli of NbC.

Total elastic moduli (kBar)							
Direction	XX	YY	ZZ	XY	YZ	ZX	
XX	6830.9842	1171.7111	1171.7111	-0.0000	-0.0000	0.0000	0.0000
YY	1171.7111	6830.9842	1171.7111	0.0000	-0.0000	0.0000	0.0000
ZZ	1171.7111	1171.7111	6830.9842	-0.0000	-0.0000	-0.0000	-0.0000
XY	-0.0000	0.0000	-0.0000	1750.3332	0.0000	0.0000	0.0000
YZ	-0.0000	-0.0000	-0.0000	0.0000	1750.3332	0.0000	0.0000
ZX	0.0000	0.0000	-0.0000	0.0000	0.0000	1750.3332	1750.3332

**Table 5**

Young's modulus, linear compressibility, shear modulus and Poisson's ratio of NbC.

NbC	Young's modulus GPa		Linear compressibility $TPa^{-1}$		Shear modulus GPa		Poisson's ratio	
	$E_{min}$	$E_{max}$	$\beta_{min}$	$\beta_{max}$	$G_{min}$	$G_{max}$	$\nu_{min}$	$\nu_{max}$
Value	440.97	648.79	1.09	1.09	175.03	282.96	0.108	0.369
Anisotropy	1.471		1.000		1.617		3.414	

**Table 6**

Surface energy of NbC(100) model.

layer	5	7	9	11	13	15
$\sigma_{\text{NbC}}(\text{J}/\text{m}^2)$	1.13	1.84	1.95	1.19	1.46	1.45

**Table 7**Surface energy of YAlO<sub>3</sub>(001) O1-terminated model.

layer	7	11	15	19	23	27	31
$\sigma_{\text{YAlO}_3}(\text{J}/\text{m}^2)$	6.81	6.75	6.65	6.44	6.37	6.34	6.35

**Table 8**Surface energy of YAlO<sub>3</sub>(001) O2-terminated model.

layer	7	11	15	19	23	27	31
$\sigma_{\text{YAlO}_3}(\text{J}/\text{m}^2)$	11.62	11.51	11.41	11.22	11.20	11.19	11.21

**Table 9**Surface energy of YAlO<sub>3</sub>(001) Y-terminated model.

layer	5	9	13	17	21	25
$\sigma_{\text{YAlO}_3}(\text{J}/\text{m}^2)$	2.10	2.09	2.09	2.08	2.07	2.07

**Table 10**Work of adhesion of YAlO<sub>3</sub>(001)/NbC(100) models.

Interface	Nb-Y	C-Y	Nb-O1	C-O1	Nb-O2	C-O2
$W_{\text{ad}}(\text{J}/\text{m}^2)$	2.031	2.299	0.789	0.458	6.399	6.558

**Table 11**Interfacial energy of YAlO<sub>3</sub>(001)/NbC(100) models.

Interface	Nb-Y	C-Y	Nb-O1	C-O1	Nb-O2	C-O2
$\gamma(\text{J}/\text{m}^2)$	1.499	0.54	7.071	7.372	6.281	6.122